ACS APPLIED ENERGY MATERIALS

www.acsaem.org
Article

Stress-Relieving Carboxylated Polythiophene/Single-Walled Carbon Nanotube Conductive Layer for Stable Silicon Microparticle Anodes in Lithium-Ion Batteries

Donghee Gueon,[#] Haoze Ren,[#] Zeyuan Sun, Bar Mosevitzky Lis, Dang D. Nguyen, Esther S. Takeuchi, Amy C. Marschilok, Kenneth J. Takeuchi, and Elsa Reichmanis*

Cite This: ACS Appl. Energy Mater. 2024, 7, 7220−7231
Read Online

ACCESS | Metrics & More | Article Recommendations | Supporting Information

ABSTRACT: Stress-relieving and electrically conductive single-walled carbon nanotubes (SWNTs) and conjugated polymer, poly[3-(potassium-4-butanoate)thiophene] (PPBT), wrapped silicon microparticles (Si MPs) have been developed as a composite active material to overcome technical challenges such as intrinsically low electrical conductivity, low initial Coulombic efficiency, and stress-induced fracture due to severe volume changes of Si-based anodes for lithium-ion batteries (LIBs). The PPBT/SWNT protective layer surrounding the surface of the microparticles physically limits volume changes and inhibits continuous solid electrolyte interphase (SEI) layer formation that leads to severe pulverization and capacity loss during cycling, thereby maintaining electrode integrity. PPBT/SWNT-coated Si MP anodes exhibited high initial Coulombic efficiency (85%) and stable capacity retention (0.027% decay per cycle) with a reversible capacity of 1894 mA h g^{-1} after 300 cycles at a current density of 2 A g^{-1}, 3.3 times higher than pristine Si MP anodes. The stress relaxation and underlying mechanism associated with the incorporation of the PPBT/SWNT layer were interpreted by quasi-deterministic and quantitative stress analyses of SWNTs through *in situ* Raman spectroscopy. PPBT/SWNT@Si MP anodes can maintain reversible stress recovery and 45% less variation in tensile stress compared with SWNT@Si MP anodes during cycling. The results verify the benefits of stress relaxation *via* a protective capping layer and present an efficient strategy to achieve long cycle life for Si-based anodes for next-generation LIBs.

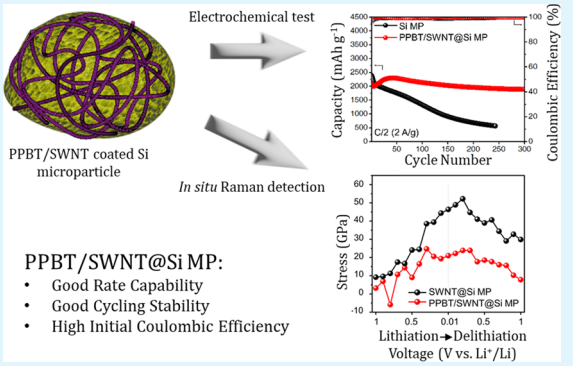

KEYWORDS: *silicon microparticles, surface chemistry, stress relaxation, single-walled carbon nanotubes, lithium-ion batteries*

1. INTRODUCTION

To support the ever-growing and expanding demand for energy for a range of applications (*i.e.*, electric vehicles, portable electronics, and grid-scale energy storage systems),[1−5] the development of advanced lithium-ion battery systems (LIBs) with high energy density, high power, and longer cycle life is essential.[1,6] Graphite, one of the most commonly available anode materials, stores energy by an intercalation mechanism ($6\ C + x\ Li + x\ e^- \rightarrow Li_xC_6\ (0 < x < 1)$) and has been widely used in commercial LIBs in spite of a low theoretical capacity of 372 mA h g^{-1}.[7] To overcome the low energy density limitations of graphite, a variety of high-capacity anode materials have been explored (*i.e.*, Si, Sn, Ge, and transition metal oxides, MnO_2, Fe_3O_4, SnO_2).[8−12] Among these options, silicon is considered one of the most promising and attractive materials due to its high theoretical capacity 4200 mA h g^{-1} ($Li_{22}Si_5$), low voltage platform (0.3 V *vs* Li/Li^+), natural abundance, low-toxicity, and environmental friendliness.[13−15]

Technical challenges, however, continue to limit the practical commercial implementation of silicon. Massive volume changes (~400%) and the low intrinsic electrical conductivity (10^{-5}−10^{-3} S cm^{-1}) of silicon induce severe pulverization and continuous accumulation of the solid electrolyte interphase (SEI) layer, leading to irreversible electrochemical reactions, delamination, and degradation of electrode performance.[16−18] The low initial Coulombic efficiency (ICE) of Si-based anodes (50−80%)[19−21] also causes approximately 20% loss of energy initially stored in the battery system. Several efforts to address these challenges have been reported.[22] For instance, zero-dimensional (0D) to two-dimensional (3D) nanostructured silicon anode materials have

Received: May 4, 2024
Revised: August 14, 2024
Accepted: August 19, 2024
Published: August 28, 2024

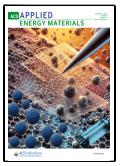

been introduced as attractive candidates, where size effects associated with particle size below 150 nm reduce stress and efficiently shorten the ion diffusion length.[23,24] While a variety of 0D Si nanoparticles,[24] one-dimensional (1D) Si nanowires,[25] two-dimensional (2D) Si nanosheets,[26] and 3D anode materials[15,27] have been developed, their intrinsically large surface area is invariably exposed to the organic electrolyte. Since it is difficult to avoid continuous decomposition of the electrolyte component, a thick SEI layer inevitably accumulates, subsequently leading to low Coulombic efficiency and poor cycle life.[28]

Another strategy encompasses modification of the surface of Si-based materials with conductive carbon (*i.e.*, crystalline/amorphous carbon,[29] carbon nanotubes,[30] and graphene[31]).[32] This approach has been widely investigated due to its effectiveness in buffering volume expansion and reducing electrical resistance. However, the production of a homogeneous carbon shell *via* processes such as hydrothermal carbonization[33] or chemical vapor deposition[34] typically involves multiple fabrication steps and may be difficult to produce at scale.[35] Further, the as-produced carbon shell is brittle and can readily break and detach from the active material surface. As a result, the active material is freshly exposed to the electrolyte, which leads to continued SEI accumulation within a hundred cycles.[36,37]

Despite pioneering work and progress in the morphological modification of Si-based anode materials, they continue to suffer from stress induced by volume expansion. Nanoparticle systems might also be incompatible with the development toward practical LIB applications due to their low tap density (~low volumetric capacity) and high specific area-induced side reactions (*e.g.*, SEI layer formation), even in light of significant progress related to prolonging cycling stability. Thus, the design of strategies with durable stress-relieving approaches that are both practical and scalable is critically required.

Herein, we present poly[3-(potassium-4-butanoate)-thiophene]/single-walled carbon nanotube (PPBT/SWNT)-coated silicon microparticles (Si MPs) (PPBT/SWNT@Si MPs) as active materials for highly stable Si-based anodes for LIB systems. The water-soluble conjugated polymer, PPBT, was selected for its ability to serve as an ion and electron conducting (10^{-5} S cm^{-1} *vs* PVDF; ~10^{-8} S cm^{-1}) physical/chemical linker to the surface of various high-capacity anode materials,[38−40] including Fe_3O_4, silicon monoxide (SiO_x) particles, and silicon nanoparticles in LIB systems.[11,41,42] In consideration of the current practical requirements for Si-based anode materials,[7,22,43] Si MPs were selected as starting materials due to their lower surface area compared to nanoscale Si materials. In addition, Si MPs are known to have high initial Coulombic efficiency and industrial compatibility.[44] With the help of PPBT, which facilitates the unraveling of entangled single-walled carbon nanotubes,[11,41,45] SWNTs were successfully attached to the surface of the active materials. PPBT carboxylate substituents were found to be chemically bound to the Si MP surface, providing an electrochemically conductive environment in intimate contact with the 1D SWNTs and Si MPs. Due to facilitated ion/electron transport kinetics, PPBT/SWNT@Si MP anodes exhibited superior capacity retention (58%) and higher reversible capacities (1715 mA h g^{-1}), even at a high current density of 8 A g^{-1} using a conventional poly(acrylic acid)/poly(vinyl alcohol) (PAA/PVA) binder system, compared to bare Si MP anodes (51%, 1335 mA h g^{-1}). The improved ICE (PPBT/SWNT@Si MP: 85% *vs* Si MP: 78%) was achieved, owing to the limited side reactions during the first cycle.

The PPBT/SWNT@Si MP anodes also demonstrated a stable cycling performance of over 300 cycles (0.027% decay ratio per cycle). The origins of the cycling stability were investigated using *in situ* Raman spectroscopy, which allowed for interrogation of the evolution of stress on the SWNTs during lithiation/delithiation. The results provided mechanistic insight into the underlying enhancement in the cycling performance of the PPBT/SWNT@Si MP anodes. The single-walled carbon nanotubes within the PPBT/SWNT@Si MP anodes consistently exhibited reversible stress recovery and 45% less tensile stress variation after the 10th cycle than the SWNT@Si MP control anodes fabricated by direct mixing of the microparticles with SWNTs. Combined, the results suggest that a well-developed conductive interface provides for efficient stress relaxation of Si-based electrodes, resulting in reversible lithiation/delithiation, low electrode resistance, and reduced SEI layer formation.

2. EXPERIMENTAL SECTION

2.1. Preparation of PPBT/SWNT@Si MPs. Silicon microparticles (0.6 g; 1−5 μm average diameter, purchased from Alfa Aesar) were added to 120 mL of 20 wt % poly(diallydimethylammonium chloride) (PDDA, purchased from Sigma-Aldrich) aqueous solution and sonicated in a water bath (purchased from Branson Ultrasonics Corp) for 3 h. The resulting PDDA@Si MPs were washed 3 times with 100 mL of deionized (DI) water to remove excess PDDA and extracted by vacuum filtration. The obtained PDDA@Si MPs were dried at 60 °C on a hot plate overnight. PDDA@Si MPs (0.27 g) were dispersed in 30 mL of DI water and sonicated in a water bath for 1 h. PPBT (30 mg; M_w: 16 kDa, polydispersity: 2.2, head-to-tail regioregularity: 89%, as purchased from Rieke Metals, Inc.) and SWNTs (15mg; Cheap Tubes Inc.) were added to 10 mL of DI water and sonicated in a water bath for 1 h. PPBT/SWNT dispersions were then added dropwise to the PDDA@Si MP aqueous dispersion and sonicated in a water bath for 1 h. The resulting dispersion was washed with 100 mL of DI water 3 times, vacuum filtrated, and dried at 80 °C on a hot plate overnight to obtain PPBT/SWNT@Si MPs. The Low-PPBT/SWNT-content anode was prepared with 0.27 g of Si, 15 mg of PPBT, and 7.5 mg of SWNT, and all other steps remained the same. The High-PPBT/SWNT-content anode was prepared with 0.27 g of Si, 45 mg of PPBT, and 22.5 mg of SWNT, and all of the other steps remained the same. SWNT@Si MPs were obtained by directly mixing and grinding SWNT with Si MPs.

2.2. Materials Characterization. A field emission scanning electron microscope (Hitachi S-4300) was used for the SEM measurements. TEM was obtained using a JEOL JEM2100. Raman spectra were obtained using a Horiba LabRAM Odyssey confocal Raman microscope equipped with an air-cooled Ar-ion laser operating at 532 nm. X-ray photoelectron spectroscopy (XPS) was performed using a Specs XPS system with an Al Kα monochromatic beam (1486.6 eV). ATR-Fourier transform infrared (ATR-FTIR) spectra were recorded on a Nicolet iS 10 FT-IR spectrometer. X-ray diffraction (XRD) patterns were obtained using a Panalytical Empyrean system; samples were scanned between 10 and 100° at a scan rate of 0.05° s^{-1}. Thermogravimetric analysis (TGA) was performed with a TA Instruments TGA Q500. Zeta potential was measured by using a Zetasizer ZS (Malvern Panalytical, Worcestershire, United Kingdom). To compare the nanoindentation results of Si MP and PPBT/SWNT@Si MP electrodes, a SteP4-NHT3 (Anton Paar TriTec) instrument was used, with applied load and release rates of 1.2 mN/min and a 10 s pause time.

2.3. Electrochemical Measurements. CR2032 coin cells (Wellcos Corporation) were assembled using Li metal foil (Honzo Chemical Corp.) as the counter electrode and a propylene membrane as a separator (Celgard 2400). A slurry was prepared comprising

https://doi.org/10.1021/acsaem.4c01132
ACS Appl. Energy Mater. 2024, 7, 7220−7231

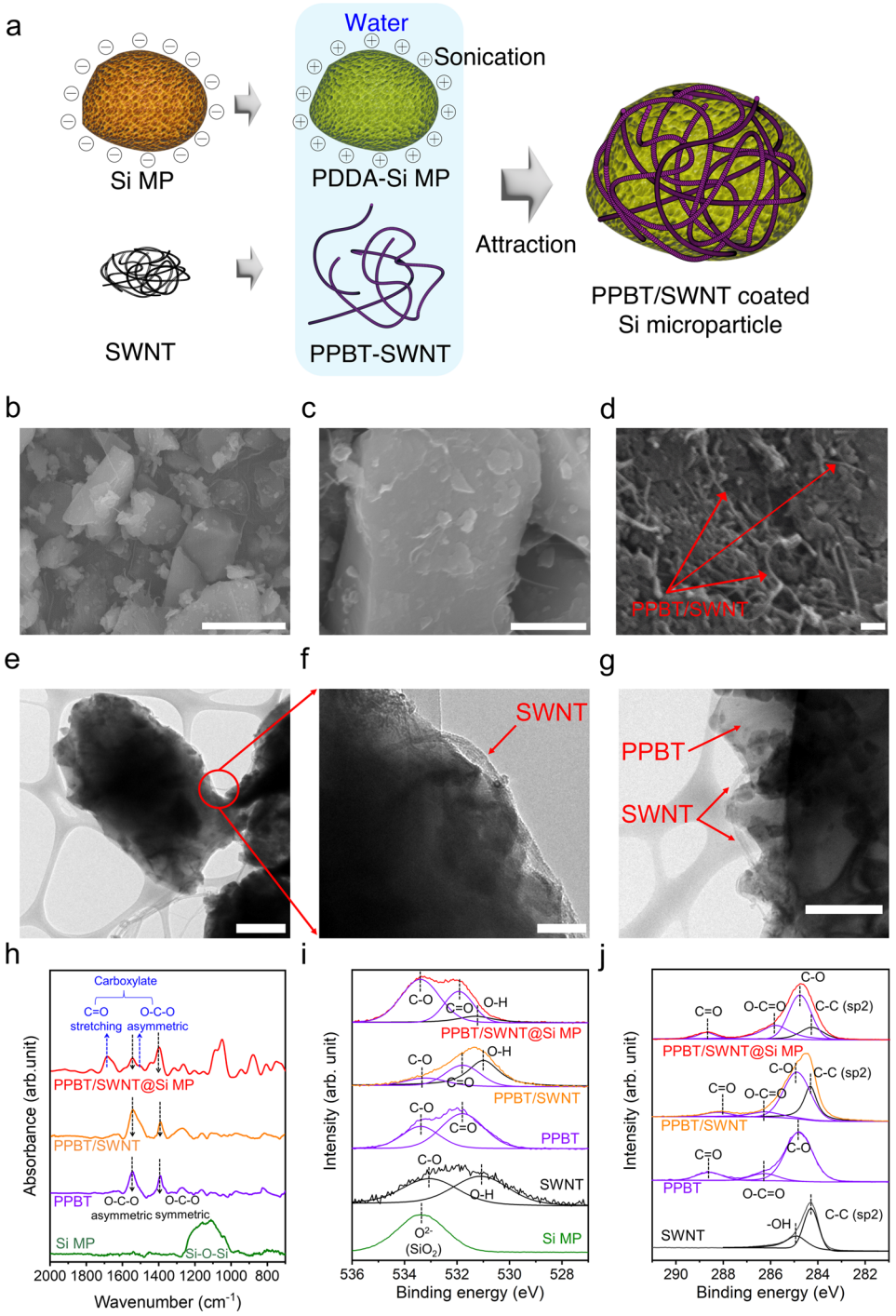

Figure 1. (a) Schematic images of fabrication steps for PPBT/SWNT@Si MPs. (b–d) Scanning electron microscope (SEM) images of PPBT/SWNT@Si MPs (scale bar: b. 5 μm, c. 1 μm, d. 100 nm). (e–g) Transmission electron microscopy images of PPBT/SWNT@Si MPs (scale bar: e. 500 nm, f. 100 nm, g. 500 nm). (h) Fourier transform infrared (FT-IR) spectra of Si MPs, PPBT, PPBT/SWNT, and PPBT/SWNT @Si MPs. (i) O 1s spectra of Si MPs, SWNT, PPBT, PPBT/SWNT, and PPBT/SWNT@Si MPs. (j) C 1s spectra of SWNT, PPBT, PPBT/SWNT, and PPBT/SWNT@Si MPs.

active material (Si MPs, or PPBT/SWNT@Si MPs), super P and mixed binder poly(acrylic acid) (PAA, Sigma, M_w ~ 250,000): poly(vinyl alcohol) (PVA, Sigma-Aldrich, M_w ~ 30,000–70,000) (PAA: PVA = 85:15) in a weight ratio of 70:15:15 with 2 mL of DI water as a solvent. The slurry was then mixed using a Pulverisette 23 (Fritsch) ball milling apparatus for 4500/s and 15 min. Working electrodes were prepared by blade-coating the electrode slurry on the Cu foil substrate (MTI Corporation, thickness: 9 μm). The mass loading of active materials for all samples was ~1 mg cm^{-2}. The as-prepared electrodes were pre-evaporated in a vacuum oven overnight and then dried at 150 °C for 1 h in a vacuum oven. The calculated specific capacitances are based on the mass of the actual active materials, excluding the SWNT, PPBT, Super P, and PAA/PVA. The electrolyte was 1 M $LiPF_6$ in a mixture of ethylene carbonate (EC)/diethyl carbonate (DEC) (1:1 v/v %) (Sigma-Aldrich, 746,746), 10 wt % fluoroethylene carbonate (FEC, Fisher TCI America) was added, and the resultant solution was mixed overnight at room temperature. CV was performed in the potential range of 0.01–1 V at

https://doi.org/10.1021/acsaem.4c01132
ACS Appl. Energy Mater. 2024, 7, 7220–7231

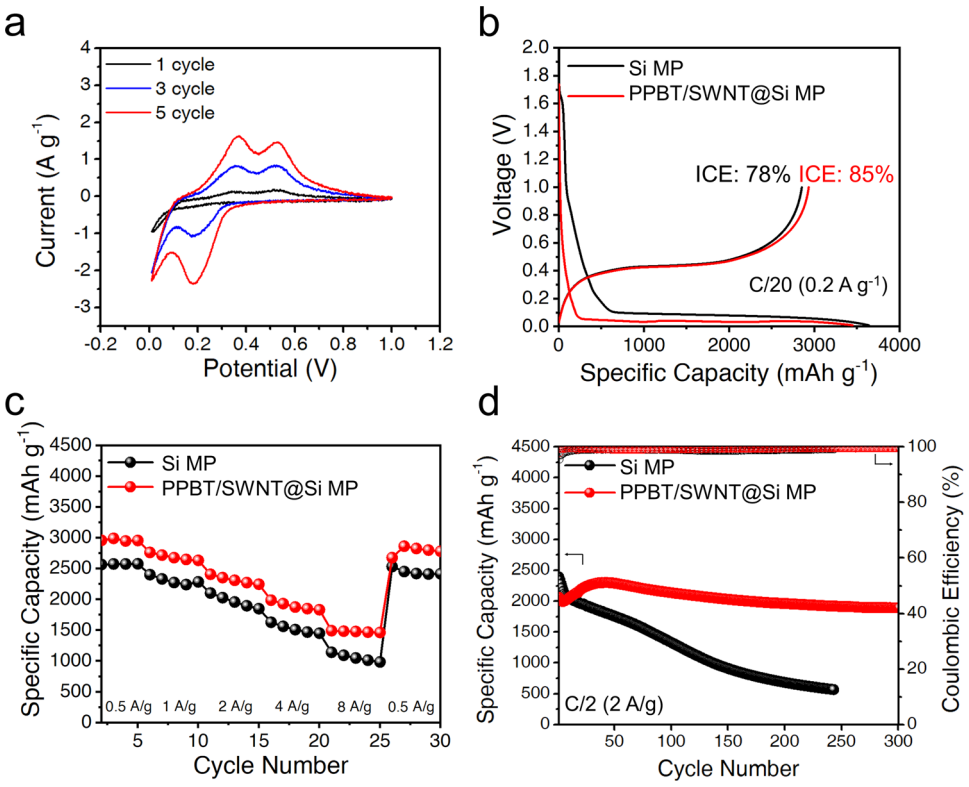

Figure 2. (a) CV profiles of PPBT/SWNT@Si MP anodes in the potential window of 0.01 to 1 V versus Li/Li^+ at a scan rate of 0.1 mV s^{-1}. (b) Charge/discharge voltage profiles of Si MP and PPBT/SWNT@Si MP anodes at a current density of 0.5 A g^{-1}. (c) Rate capabilities of Si MP and PPBT/SWNT@Si MP anode cells measured at various current densities from 0.5 to 8 A g^{-1}. (d) Cycle performances of Si MP and PPBT/SWNT@Si MP anodes at a current density of 2 A g^{-1} for 300 cycles.

a rate between 0.1 and 0.5 mV s^{-1}. Electrochemical impedance spectroscopy (EIS) was performed in the frequency range of 1 MHz−0.1 Hz. A 4-point Probe test was performed using Keithley 2100. The anode slurry was coated on the glass substrate and cut into 2 cm × 2 cm samples after drying. Each electrode was tested at five points, and the average value was taken.

2.4. *In Situ* Raman Sample Preparation and Spectroscopic Measurements. For the PPBT/SWNT@Si MPs used in the *in situ* Raman experiments, 0.3 g of PDDA@Si MPs was dispersed in 30 mL of DI water and sonicated in a water bath for 1 h. PPBT (50 mg) and SWNTs (25 mg) were added to DI water (10 mL) and sonicated in a water bath for 1 h. PPBT/SWNT dispersions were added dropwise to the PDDA@Si MP aqueous dispersion and sonicated in a water bath for 1 h. The dispersion was extracted by vacuum filtration and dried at 80 °C on a hot plate overnight to obtain PPBT/SWNT@Si MPs. The SWNT@Si MPs were prepared following the same steps using 0.3 g of PDDA@Si MPs and 25 mg of SWNTs.

The binder was prepared by mixing PAA and PVA in a mass ratio of 85:15, and the binder solution solid content was 10 wt %. The electrode consisting of PPBT/SWNT@Si MPs (or SWNT@Si MPs), super P, and binder (PAA/PVA = 85:15) was 70:20:10 in mass ratio, and DI water was used as a solvent. The slurry was mixed using a Pulverisette 23 (Fritsch) ball milling apparatus for 4500/s and 15 min. *In situ* Raman electrodes were prepared by blade-coating electrode slurry on the Cu foil substrate. The mass loading of active materials for all *in situ* Raman samples was ∼1 mg cm^{-2}. These prepared electrodes were pre-evaporated in a vacuum oven overnight and then dried at 150 °C for 1 h in a vacuum oven. The electrolyte was 1 M $LiPF_6$ in a mixture of ethylene carbonate (EC)/diethyl carbonate (DEC) (1:1 v/v %) (Sigma-Aldrich, 746746), 10 wt % fluoroethylene carbonate (FEC, Fisher TCI America) was added and the resultant solution was mixed overnight at room temperature. The PPBT/SWNT@Si MP and SWNT@Si MP anodes were assembled into an *in situ* Raman cell (ECC-Opto-10) purchased from EL-CELL. A Gamry interface 1000 potentiostat was used to perform CV scanning (0.1 mV s^{-1}). Raman spectra were obtained using a Horiba LabRAM Odyssey confocal Raman microscope with a 532 nm excitation laser source in backscattering geometry. The spectra were measured through a 50× objective. The laser power was set at 5% power (6.9 mW) under all conditions to avoid photothermal effects and sample degradation. The scanned spectral region ranged between 100 and 1799 cm^{-1}. A silicon substrate was used for the calibration. All spectra were collected using LabSpec 6 software and further deconvoluted through Origin 2023b software.

3. RESULTS AND DISCUSSION

3.1. PPBT/SWNT@Si MP Preparation and Materials Characterization. Figure 1a schematically illustrates the process for the preparation of PPBT/SWNT@Si MPs. While they are known to exhibit less stable electrode integrity during cycling and lower Li^+ diffusion than that of Si nanoparticles, commercial Si MPs with a diameter ranging from 1 to 5 μm (Figure S1) were used as the high-capacity materials due to their industrial compatibility (*e.g.*, low-cost manufacturing, higher tap density for higher volumetric capacities, lower specific surface area reducing side reactions, *etc.*) that overcomes intrinsic limitations of nano-Si materials.[44] PPBT with a conjugated backbone and carboxylate functionalized side chain was selected to easily disperse bundled electron-rich SWNTs (Figure S2). The conjugated polythiophene backbone physically interacts with the electron-rich SWNT surface through noncovalent $\pi-\pi$ interactions (Figure S3). Poly(diallydimethylammonium chloride) (PDDA) pretreatment of the Si MPs induced the Si MP surface to become positively charged, leading to an electrostatic affinity between the Si MPs and negatively charged PPBT/SWNTs upon dropwise

https://doi.org/10.1021/acsaem.4c01132
ACS Appl. Energy Mater. 2024, 7, 7220−7231

addition into the Si MP dispersion. The reversal of the surface charge of PPBT/SWNT@Si MPs to a negative charge suggests that the PDDA layer originally present on the Si MP surface has been replaced by PPBT/SWNT (Figure S4).[45,46]

Figure 1b–d presents scanning electron microscope (SEM) images of PPBT/SWNT@Si MPs, demonstrating the presence of a well-attached fibrous SWNT structure on the Si MP surface. Figures 1e–g and S5 showcase transmission electron microscopy (TEM) images of PPBT/SWNT@Si MPs and Si MPs, respectively. These images reveal a distinctive amorphous PPBT layer on the surface of the silicon particles. The SWNTs are observed to adhere to and wrap onto the Si MPs, most likely facilitated by the $\pi-\pi$ interactions between the SWNTs and the PPBT backbone. The energy-dispersive spectroscopy (EDS) mapping images corresponding to the TEM data are shown in Figure S6. X-ray diffraction (XRD) results confirm that the Si MPs maintain their structural integrity upon PPBT/SWNT attachment (Figure S7). Further, the presence of chemical interactions between the PPBT/SWNTs and Si MPs was verified *via* Fourier transform infrared (FT-IR) spectroscopic analysis (Figure 1h). Vibrational bands appearing at ~1558 and 1398 cm^{-1} are indicative of PPBT −O−C−O− asymmetric and symmetric stretching vibrations, respectively. In the case of PPBT/SWNT@Si MPs, a new carboxylate peak is apparent at ~1716 cm^{-1} corresponding to C═O stretching, and that at ~1516 cm^{-1} is assigned to the O−C−O asymmetric stretching mode. A shoulder is also evident, split from an ~1558 cm^{-1} band, which is associated with the formation of carboxylate moieties bound to hydroxyl groups present on the surface of metal oxide-based active materials (*e.g.*, Fe_3O_4 and SiO_x).[11,45] The mixed conduction properties of PPBT,[38,39] coupled with its ability to physically and chemically bind to SWNTs and Si MPs, respectively, enable the creation of facile electrical conduction pathways. X-ray photoelectron spectroscopy (XPS) results support the presence of PPBT/SWNTs on the Si MPs. The Si MP peak at ~533 eV in Figure 1i points to an abundance of surface oxygen groups that are available for reaction with the polythiophene carboxylate substituents to form a stable PPBT/SWNT capping layer,[41,42] while the O 1s and C 1s XPS spectra of PPBT/SWNT@Si MPs exhibited peaks corresponding to C−O and C═O, consistent with the presence of PPBT (Figure 1i,j).[41,47] Thermogravimetric analysis (Figure S8 and Table S1) was performed to confirm the weight ratio of Si MPs in PPBT/SWNT@Si MPs (88.6 wt % Si MPs).

3.2. Electrochemical Performance. The electronic conductivity of the PPBT/SWNT@Si MP, Si MP, and their respective anodes was measured using the four-point probe method (Figure S9). The results indicate that with the PPBT/SWNT coating, the PPBT/SWNT@Si MPs and the anodes fabricated from the respective materials exhibit improved electrical conductivity compared with the Si MPs. The electrode peel-off experiment conducted on both Si MP and PPBT/SWNT@Si MP anodes (Figure S10) demonstrated that the PPBT/SWNT@Si MP anode is more resistant to delamination than the control. The electrochemical characteristics of Si MP and PPBT/SWNT@Si MP anodes were evaluated in a half-cell configuration (Figures 2, S11, and S12), where the as-prepared anodes were assembled using a polypropylene separator and lithium metal as a counter electrode to evaluate the impact of the PPBT/SWNT coating. Cyclic voltammetry (CV) of the PPBT/SWNT@Si MP system was performed in a range of 0.01−1 V *vs* Li^+/Li at a sweep rate of 0.1 mV s^{-1} (Figure 2a). The cathodic peaks appearing in the range of 0.01−0.2 V are associated with the initial insertion of Li^+ into the silicon crystal lattice, forming amorphous lithium silicide (Li_xSi, lithiation) during the reduction process. The increasing peak intensity observed during subsequent cycles at 0.2 V represents a reversible lithiation of amorphous Si to Li_xSi.[48,49] The anodic peaks at 0.3 and 0.5 V reflect the formation of amorphous Si from the Li_xSi phase during oxidation.[50] Over 5 cycles, the Si MPs were gradually activated, as evidenced by the increasing intensity of the peaks.

CV scans of both anodes at potential scan rates in the range of 0.2−0.5 mV s^{-1} between 1 and 0.01 V *vs* Li^+/Li are presented in Figures S11 and S12. These compare the relative diffusion coefficient of Si MP and PPBT/SWNT@Si MP anodes by the Randles-Sevcik equation based on the relationship of scan rate *vs* peak current (I_p), where n, A, D_o, and C_o refer to the number of electrons per reaction species (1 for Li^+), electrode surface area, diffusion coefficient of Li^+ in the electrode, and bulk concentration of Li^+, respectively (eq 1).[51] Both Si MP and PPBT/SWNT@Si MP anodes exhibited a linear relationship between I_p and the square root of the scan rate ($v^{1/2}$), as lithiation/delithiation is diffusion-limited in both systems. The slope proportional to D_o is steeper for PPBT/SWNT@Si MP electrodes *vs* their Si MP counterparts (Figure S13), indicating that lithium-ion diffusion is enhanced upon PPBT/SWNT modification. The results suggest improved lithium alloying/dealloying kinetics within the PPBT/SWNT@ Si MP electrode.[52,53]

$$I_p = 2.69 \times 10^6 \times n^{3/4} \times A \times D_o^{1/2} \times v^{1/2} \times C_o \quad (1)$$

Galvanostatic charge/discharge tests were performed in the potential range of 0.01−1 V *vs* Li/Li^+ voltage window typically used for Si-based anodes[54] at various current densities between 0.5 and 8 A g^{-1}. The PPBT/SWNT@Si MP system exhibited a comparable discharge capacity of 3447 mA h g^{-1} and a higher ICE of 85% than the Si MP anodes (78% ICE, Figure 2b) at a current density of 0.5 A g^{-1}. ICE of the PPBT/SWNT@Si MP anode compares favorably to previously reported Si-based anodes (Table S2). A voltage plateau observed at ~0.8−0.9 V *vs* Li/Li^+ on the first lithiation curve corresponds to electrolyte decomposition and formation of the SEI layer on the active material surfaces.[55] Superior ICE of the PPBT/SWNT@Si MP anodes could be attributed to negligible SEI formation and facilitated electron and ion transport after incorporation of the PPBT/SWNT coating.

From a performance perspective, next-generation LIBs require high-capacity retention at a high current density. In Figure 2c, benefiting from the electrically and ionically conductive PPBT/SWNT layer, PPBT/SWNT@Si MP anodes exhibited better discharge capacity and capacity retention than anodes prepared from Si MPs over a wide range of current densities (0.5 to 8 A g^{-1}). Even at a high current density of 8 A g^{-1}, the PPBT/SWNT@Si MP anodes retained 1715 mA h g^{-1} (58% retention), which outperforms the Si MP-based control (1335 mA h g^{-1}, 51% retention). To achieve real-world application standards, stable cycling over hundreds of cycles is essential. PPBT/SWNT@Si MP anodes exhibited a stable cycling performance at a current density of 2 A g^{-1} for 300 cycles. Notably, as presented in Figure 2d, the observed capacity decay rate for the PPBT/SWNT@Si MP anodes (0.027% capacity decay per cycle, 300 cycles) is an order of

https://doi.org/10.1021/acsaem.4c01132
ACS Appl. Energy Mater. 2024, 7, 7220−7231

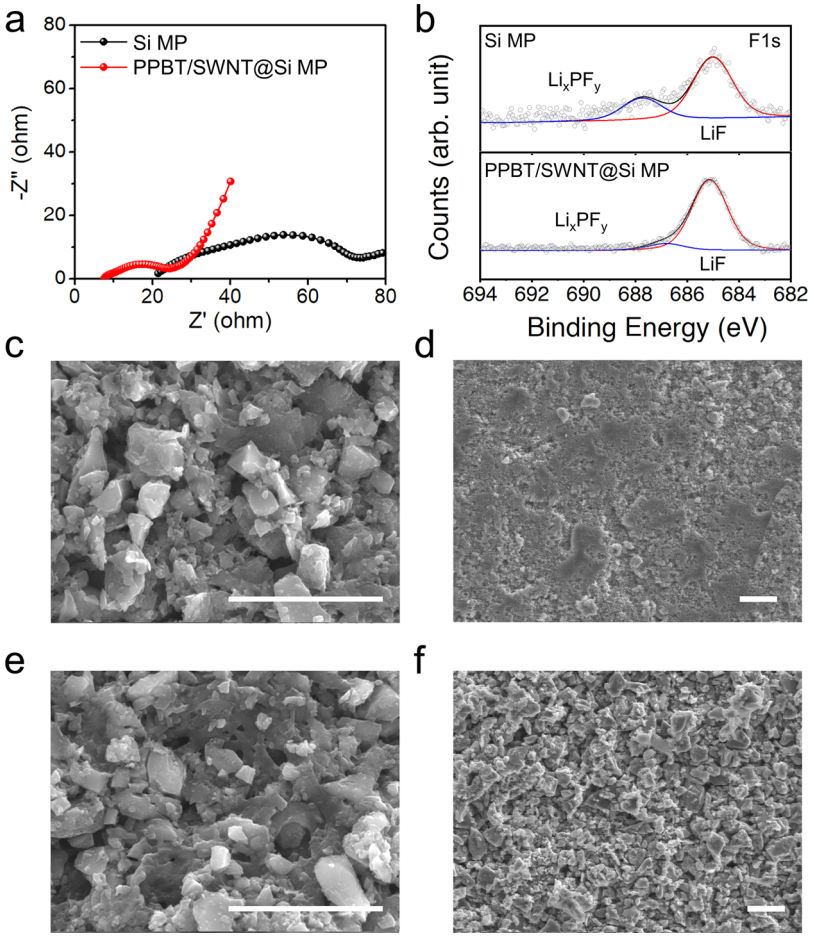

Figure 3. (a) EIS spectra of Si MP and PPBT/SWNT@Si MP anodes after cycling. (b) F 1s peak of Si MP and PPBT/SWNT@Si MP anodes after cycling. SEM images of Si MP anodes (c) before and (d) after cycling. SEM images of PPBT/SWNT@ Si MP anodes (e) before and (f) after cycling (scale bar: 10 μm).

magnitude lower than either Si MP (0.314% capacity decay per cycle) or SWNT@Si MP anodes (0.266% capacity decay per cycle, Figure S14); even under high-mass loading conditions (~2 mg cm^{-2}) (Figure S15), PPBT/SWNT@Si MP anodes exhibit superior cycling stability. Additionally, SEM cross-section images for PPBT/SWNT@Si MP and Si MP anodes were obtained. As presented in Figure S16, the PPBT/SWNT@Si MP electrodes exhibited a negligible thickness change after cycling, while the Si MP electrodes demonstrated a significant increase in thickness. This indicates that the PPBT/SWNT coating effectively restricts the volume change of silicon during cycling, preventing silicon particle pulverization and enhancing the cycling performance of the electrodes. Electrode capacity is influenced by various factors, including current density and active material mass loading (thickness);[56,57] however, despite these variables, PPBT/SWNT@Si MP electrodes exhibited an attractive initial capacity and a decay rate that surpasses that of the widely studied nanosilicon alternatives, traditionally viewed as a more stable anode active material (Table S3).[58] Further, the PPBT/SWNT@Si MP system maintained reversible voltage profiles (Figure S17) and a high discharge capacity of 1894 mA h g^{-1} over 300 cycles, which is 3.3 times higher than that of the Si MP control (568 mA h g^{-1}, 243 cycles). In the latter case, the poor cycling stability and low discharge capacity were most likely induced by pulverization of Si MPs from the current collector, whereby stress caused by large volume expansion of Si MPs during lithiation/delithiation is known to easily degrade electrode structural integrity.[59,60] The anode cycling performance of electrodes prepared with different PPBT/SWNT coating layer contents is shown in Figure S18. The High-PPBT/SWNT-content anode exhibits degradation after 40 cycles. Enhancing the amount of the PPBT/SWNT layer may have initially improved cycling stability, but the subsequent decline was more rapid. Conceivably, the higher PPBT/SWNT coating content layer possesses more crystalline regions that restrict lithium-ion percolation pathways, which increase electrode tortuosity and thereby restrict ion transfer. Combined, these factors lead to the formation of a more substantial SEI layer during cycling (Figure S19).[61]

Electrochemical impedance spectroscopy (EIS) provides clear evidence of electrode resistance, which is strongly related to the formation of the insulating SEI layer, especially for Si-based anodes. Figure 3a presents the EIS spectra of the Si MP and PPBT/SWNT@Si MP systems after 50 cycles. Two semicircles in the high- and medium-frequency regions indicate the as-formed SEI layer (R_{SEI}) and the charge transfer resistance (R_{ct}). After cycling, PPBT/SWNT@Si MP anodes show much lower R_{SEI} than the Si MP counterparts, pointing to less SEI layer formation during repeated volume changes of Si and the newly exposed surface of fractured Si MPs in the presence of PPBT/SWNTs.[62] The slope of a straight line,

https://doi.org/10.1021/acsaem.4c01132
ACS Appl. Energy Mater. 2024, 7, 7220−7231

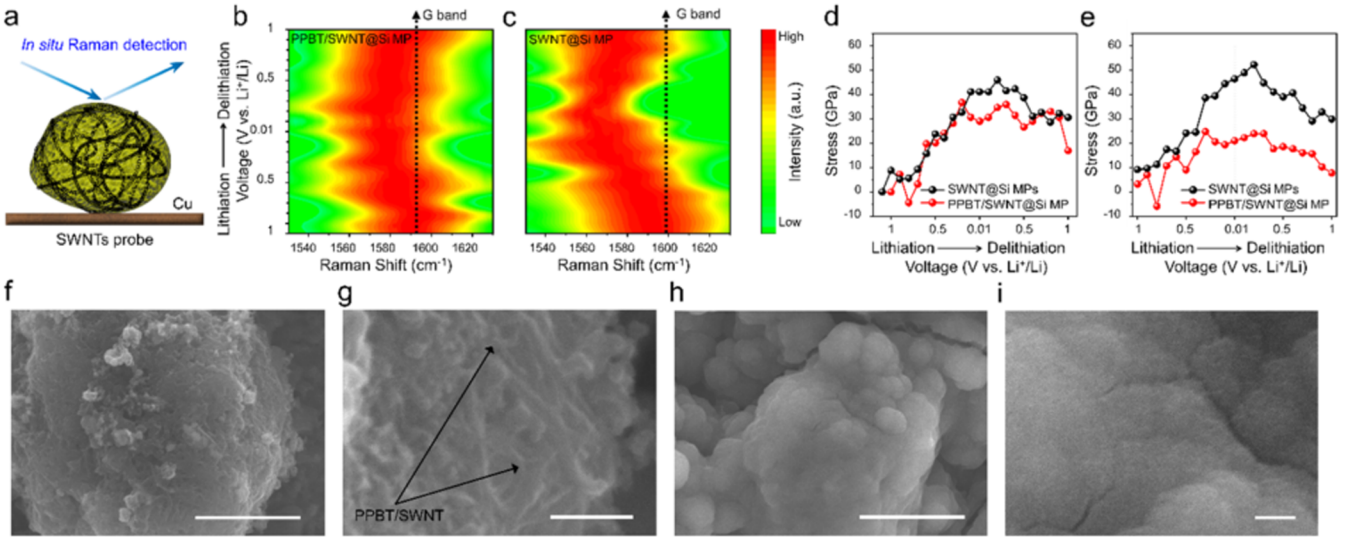

Figure 4. (a) Schematic image of stress monitoring using Raman spectroscopy. The G-band positions in the *in situ* Raman spectra for (b) PPBT/SWNT@Si MP and (c) SWNT@Si MP during cycling. The G-band shifts and corresponding strain for the SWNTs in the PPBT/SWNT@Si MP and SWNT@Si MP anodes during (d) the initial and (e) the 10th cycle. SEM images of PPBT/SWNT@ Si MP anodes (f, g) and SWNT@Si MP anodes (h, i) after *in situ* Raman analysis. (Scale bar: f, h, 2 μm; g, i, 200 nm).

referred to as the Warburg impedance region, is much higher than that of the Si MP anodes, indicating faster Li^+ ion diffusion for the PPBT/SWNT modified system.[63]

The electrochemical results strongly suggest that the surrounding electrically conductive PPBT/SWNT layer, with its 3D networked fibrous structure, not only affords stable capacity retention but also plays a key role in reducing resistance and SEI formation. Thus, the surface chemical composition and morphology of the Si MP and PPBT/SWNT@Si MP anodes were investigated by XPS and SEM before and after cycling to gain additional information related to electrode resistance and the degree of degradation. The XPS peaks appearing at 685 and 687 eV in the F 1s spectrum (Figure 3b) are attributed to the LiF and Li_xPF_y species. Reduction of fluoroethylene carbonate (FEC) and decomposition of $LiPF_6$ induce the formation of LiF and Li_xPF_y, respectively. A higher integrated intensity ratio of LiF to Li_xPF_y indicates the presence of a thinner, denser SEI layer with high shear modulus and low Li^+ diffusion barrier of ~0.17 eV, which are desirable characteristics to stabilize anode integrity.[64−66] The integrated intensity ratio of LiF to Li_xPF_y for the PPBT/SWNT@Si MP anodes is 4 times higher than that for Si MP anodes after 50 cycles, supporting less SEI layer formation and more stable cyclability of the electrode in the presence of the PPBT/SWNT layer. Stable SEI formation on the PPBT/SWNT@Si MP anodes is also supported by SEM imaging after cycling. The cycled PPBT/SWNT@Si MP anodes show less SEI layer formation compared with the Si MP counterparts, exhibiting thick SEI formation (Figure 3c−f). A thick and uneven SEI layer, which causes poor electron and Li^+ transport, indicates more consumed electrolytes in the Si MP anodes, leading to poor cycling stability.

From a practical point of view, a LIB full cell was tested by combining a PPBT/SWNT@Si MP anode with a Li-$(Ni_{0.5}Co_{0.2}Mn_{0.3})O_2$ (NCM523) cathode. The full cell was tested in the voltage range 2.8−4.3 V at a 0.2 C rate. The full cell delivered a high initial discharge capacity of 150 mA h g^{-1} and stable capacity retention of 80% for 50 cycles (Figure S20), confirming that PPBT/SWNT@Si MP represents a promising anode material for integration into practical LIB systems.

3.3. *In Situ* Raman Spectroscopy Revealing the Stress Relaxation during Cycling. The mechanism supporting the superior cycling stability of the PPBT/SWNT@Si MP anode was elucidated by using *in situ* Raman spectroscopy (Figure 4a). As verified by Bai and co-workers, an 8 cm^{-1} G-band shift (ΔG) approximately corresponds to 1% strain in a single carbon nanotube.[67] Using this value in conjunction with the theoretical Young's modulus of a single carbon nanotube, ~1.1 TPa, enables qualitative analysis of stress within the composite anode.[67,68] A decrease in the G-band frequency is indicative of an increase in strain, representing C−C bond length elongation. Conversely, an increase corresponds to the relaxation of residual strain, with commensurate C−C bond length contraction.[67] Building on this understanding of the stress-induced changes, SWNT@Si MPs (Figure S21) were prepared to serve as a control for PPBT/SWNT@Si MPs for comparative studies to validate the role and impact of PPBT. Variations in stress experienced by SWNTs within both systems were investigated during lithiation and delithiation, and stress was calculated using eqs S3 and S4 (see the Supporting Information).

During lithiation, Si MP volume expansion clearly led to shifts in the SWNT Raman G-band that are associated with changes in stress experienced by the nanotubes (Figure 4b−e). The PPBT/SWNT@Si MP and SWNT@Si MP anode G-band position during the initial cycle is presented in Figure 4b,c. For both electrodes, the band was observed to shift during the CV scanning process (voltage range from 1 to 0.01 V *vs* Li/Li^+), which indicates that SWNTs in both anodes undergo stress variations during lithiation and delithiation induced by Si MP volume changes. PPBT/SWNT@Si MP anodes exhibited a smaller deviation compared with the control, suggesting that incorporation of PPBT/SWNTs alleviates stress within the system.

Using the center of the G-band under open-circuit voltage (OCV) conditions as a reference point to analyze the SWNT G-band shifts, we derived the associated stress at different

https://doi.org/10.1021/acsaem.4c01132
ACS Appl. Energy Mater. 2024, 7, 7220−7231

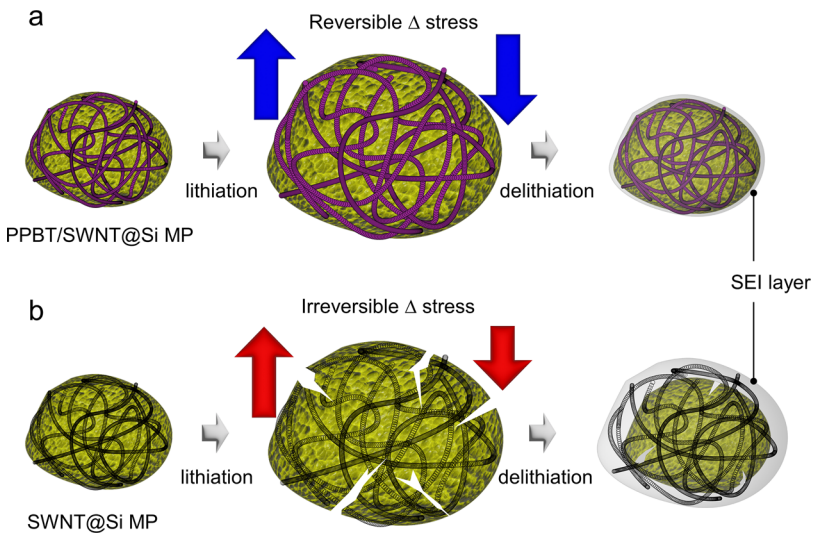

Figure 5. Schematic representation of SEI formation and morphological behavior of (a) PPBT/SWNT@Si MP and (b) SWNT@Si MP during cycling.

potentials. During the initial lithiation (Figure 4d), stress increased upon application of an external voltage, whereby considerably lower stress was experienced by PPBT/SWNT@Si MP anodes (29.0 GPa) relative to SWNT@Si MP anodes (41.1 GPa) at a fully lithiated Si MP state (0.01 V). During the first delithiation, the stress associated with the PPBT/SWNT@Si MP anodes receded to 16.9 GPa, while a large residual stress of 30.6 GPa remained in the SWNT@Si MP anode at the fully delithiated state of Si MPs (1 V). These results suggest that the PPBT/SWNT system may undergo reversible volume recovery and possess enhanced stress tolerance to volume expansion compared to the control. At subsequent cycles (Figure S22), residual stress associated with the PPBT/SWNT@Si MP electrode became almost nonexistent, suggesting that SWNTs in the PPBT/SWNT@Si MP electrode recovered to their pristine state. This indicates that the ion trapping and volumetric changes in the PPBT/SWNT@Si MP anode are rendered reversible, a finding in line with the higher initial Coulombic efficiency observed for PPBT/SWNT@Si MP electrodes (*vide supra*). During the 10th cycle (Figure 4e), a pronounced difference in stress was experienced by SWNTs incorporated in the two anodes. In the PPBT/SWNT@Si MP case, the stress was 21.0 GPa, while SWNT@Si anodes experienced 46.4 GPa stress when fully lithiated. SWNTs in PPBT/SWNT@Si MP anodes exhibited a significantly higher degree of reversible stress recovery, returning to 7.8 GPa after the delithiation process, while stress in the control remained high. Nanoindentation tests on PPBT/SWNT@Si MP and Si MP anodes were performed to further investigate the anode mechanical properties (Figure S23). The PPBT/SWNT@Si MP electrode exhibited a lower indentation depth at a given force compared to its Si MP counterpart. This indicates that the PPBT/SWNT@Si MP electrode exhibited lower irreversible deformation after the loading and unloading process, suggesting better accommodation of the expansion and contraction of Si MPs within the PPBT/SWNT@Si MP anode.

Based on the results, the incorporation of a PPBT layer that effectively links SWNTs to the active material surface alleviates stress induced by the strain associated with volume expansion, which ultimately leads to the deterioration of electrode integrity. *Ex-situ* SEM analysis of the anodes after Raman analysis provides added insight into the phenomenon. Advantageously, the SEI layer formed in the case of PPBT/SWNT@Si MP anodes was considerably thinner (Figure 4f,g) than that formed in the SWNT@Si electrodes (Figure 4h,i). Given that under large stress, a thick SEI accelerates the detachment of the conductive SWNT network from the active material,[56] the differences in the SEI help explain the observed irreversible stress recovery of the electrode in the absence of PPBT.

Through the stable cycle life, reversible SEI layer formation, and effective stress-relieving properties of PPBT/SWNT@Si MP anodes, the positive impact of PPBT incorporation into composite electrodes for energy storage applications was verified. PPBT not only facilitates the debundling of SWNTs but also serves as a bridge to connect the SWNTs to the Si MP surfaces. It has been suggested that the intrinsically weak adhesive forces between silicon and carbon nanotubes result in facile slippage between the carbon nanotubes and silicon, leading to structural collapse.[69] By linking the two components through chemical bonding to the carboxylate side chain of PPBT, stress due to lithiation/delithiation was effectively reduced, enabling prolonged cycle life, reversible capacity, and thinner SEI layer formation.

A schematic illustration of SEI formation and the morphological behavior is depicted in Figure 5a,b. During lithiation, the Si MPs underwent severe volume expansion, while the robust chemically bound PPBT/SWNT network surrounding the active materials in the PPBT/SWNT@Si MP anodes imparted significant mechanical stability, curbed volumetric changes, and minimized continuous SEI formation. From a mechanistic perspective, the stress exerted by volume expansion is evenly distributed through the SWNTs. For the SWNT/Si MP system (Figure 5a), after lithiation and upon delithiation, the expanded volume leads to SWNTs being stretched longitudinally, where Si MP volume decreases, but SWNT recovery lags lithiation. Over prolonged cycling, strong binding between the SWNT and Si MP surfaces in PPBT/SWNT@Si MP anodes ensures swift recovery to the original state. On the other hand, the lag perpetually accumulates in the

https://doi.org/10.1021/acsaem.4c01132
ACS Appl. Energy Mater. 2024, 7, 7220−7231

SWNT@Si MP anodes, eventually leading to structural collapse and pulverization of the Si MPs (Figure 5b).

4. CONCLUSIONS

A stress-relieving electroconductive PPBT/SWNT coating for Si MPs was developed, whereby the resultant PPBT/SWNT@Si MP anodes achieved a stable cycling performance with reduced SEI layer formation. The PPBT/SWNT capping layer was chemically bound to the active material surface and provided an electrically conductive interface that maintained close contact between SWNTs and the active material surface. Fibrous structures with stable conjugated polymer bridges provided for a highly electronically conducting environment exhibiting reduced stress during lithiation/delithiation. The PPBT/SWNT@Si MP anodes exhibited stable capacity retention of 92% over 300 cycles, a high capacity of 1894 mA h g^{-1} at a high current density of 2 A g^{-1}, and a high ICE of 85% at a current density of 0.5 A g^{-1}, which are challenging but required characteristics for Si-based anode materials. Furthermore, through a quantitative study of the correlation of the SWNT *in situ* Raman signal to electrode mechanical properties (*i.e.*, tensile stress), the degree of stress relaxation was determined to be significantly higher for the PPBT/SWNT@Si MP system. The observed reversible stress recovery and 45% lower degree of stress evolution due to the incorporation of the PPBT/SWNT capping layer directly provided superior electrochemical performance. The results identify a key parameter, namely, stress relaxation properties, to consider in the design of advanced active materials and protective capping layers that can be directly evaluated *via in situ* nondestructive analysis techniques. The PPBT/SWNT capping layer presents a promising, practical, applicable strategy for the development of long-cycle life Si-based anodes for next-generation LIB technologies.

■ ASSOCIATED CONTENT

Supporting Information

The Supporting Information is available free of charge at https://pubs.acs.org/doi/10.1021/acsaem.4c01132.

SEM, TEM, and EDS mapping images of PPBT/SWNT@Si MP, Si MP, and anodes; ζ-potential distributions of Si MPs, PDDA pretreated Si MPs, and PPBT/SWNT@Si MPs; XRD spectrum of PPBT/SWNT@Si MP and Si MP; TGA profile of PPBT, SWNT, Si MP, and PPBT/SWNT@Si MP; 4-point probe measurement of the PPBT/SWNT@Si MP, Si MP, and anodes; peel-off experiment images of PPBT/SWNT@Si MP and Si MP anodes; CV profiles of PPBT/SWNT@Si MP and Si MP anodes at a various scan rate; relationship of peak current and the square root of scan rate for anodic peaks of PPBT/SWNT@Si MP and Si MP anodes; cycling data of SWNT@Si MP anodes, high-mass loading SWNT@Si MP and PPBT/SWNT@Si MP anodes, and with different amounts of coating of PPBT/SWNT anodes; and full-cell cycling data of NCM523//PPBT/SWNT@Si MP electrodes (PDF)

■ AUTHOR INFORMATION

Corresponding Author

Elsa Reichmanis − *Department of Chemical and Bimolecular Engineering, Lehigh University, Bethlehem, Pennsylvania 18015, United States;* orcid.org/0000-0002-8205-8016; Email: elr420@lehigh.edu

Authors

Donghee Gueon − *Department of Chemical and Bimolecular Engineering, Lehigh University, Bethlehem, Pennsylvania 18015, United States;* orcid.org/0000-0001-8347-3409

Haoze Ren − *Department of Chemical and Bimolecular Engineering, Lehigh University, Bethlehem, Pennsylvania 18015, United States;* orcid.org/0000-0002-0450-3962

Zeyuan Sun − *Department of Chemical and Bimolecular Engineering, Lehigh University, Bethlehem, Pennsylvania 18015, United States;* orcid.org/0000-0003-0045-2392

Bar Mosevitzky Lis − *Department of Chemical and Bimolecular Engineering, Lehigh University, Bethlehem, Pennsylvania 18015, United States;* orcid.org/0000-0001-5793-5358

Dang D. Nguyen − *Department of Chemical and Bimolecular Engineering, Lehigh University, Bethlehem, Pennsylvania 18015, United States;* orcid.org/0009-0005-2959-4820

Esther S. Takeuchi − *Interdisciplinary Science Department, Brookhaven National Laboratory, Upton, New York 11973, United States; Institute of Energy: Sustainability, Environment and Equity, Stony Brook University, Stony Brook, New York 11794, United States; Department of Material Science and Chemical Engineering and Department of Chemistry, Stony Brook University, Stony Brook, New York 11794, United States;* orcid.org/0000-0001-8518-1047

Amy C. Marschilok − *Interdisciplinary Science Department, Brookhaven National Laboratory, Upton, New York 11973, United States; Institute of Energy: Sustainability, Environment and Equity, Stony Brook University, Stony Brook, New York 11794, United States; Department of Material Science and Chemical Engineering and Department of Chemistry, Stony Brook University, Stony Brook, New York 11794, United States;* orcid.org/0000-0001-9174-0474

Kenneth J. Takeuchi − *Interdisciplinary Science Department, Brookhaven National Laboratory, Upton, New York 11973, United States; Institute of Energy: Sustainability, Environment and Equity, Stony Brook University, Stony Brook, New York 11794, United States; Department of Material Science and Chemical Engineering and Department of Chemistry, Stony Brook University, Stony Brook, New York 11794, United States;* orcid.org/0000-0001-8129-444X

Complete contact information is available at: https://pubs.acs.org/10.1021/acsaem.4c01132

Author Contributions

#D.G and H.R. contributed equally to this work.

Notes

The authors declare no competing financial interest.

■ ACKNOWLEDGMENTS

This work was performed as part of the Center for Mesoscale Transport Properties, an Energy Frontier Research Center supported by the U.S. Department of Energy, Office of Science, Basic Energy Sciences, under award #DE-SC0012673. E.R. also appreciates support from Lehigh University through funds associated with the Carl Robert Anderson Chair in Chemical Engineering. E.S.T. acknowledges support as the William and Jane Knapp Chair for Energy and the Environment at Stony Brook University. The authors thank the

characterization facilities associated with the Lehigh University Institute for Functional Materials and Devices and appreciate access to the Professor Israel Wachs group Raman facilities and assistance from Han Li and Yiman Xu with experimental details.

REFERENCES

(1) Kim, N.; Kim, Y.; Sung, J.; Cho, J. Issues impeding the commercialization of laboratory innovations for energy-dense Si-containing lithium-ion batteries. *Nat. Energy* **2023**, 921−933.
(2) He, W.; Guo, W.; Wu, H.; Lin, L.; Liu, Q.; Han, X.; Xie, Q.; Liu, P.; Zheng, H.; Wang, L. Challenges and recent advances in high capacity Li-rich cathode materials for high energy density lithium-ion batteries. *Adv. Mater.* **2021**, *33* (50), No. 2005937.
(3) Kim, T. H.; Park, J. S.; Chang, S. K.; Choi, S.; Ryu, J. H.; Song, H. K. The current move of lithium ion batteries towards the next phase. *Adv. Energy Mater.* **2012**, *2* (7), 860−872.
(4) Zhang, X.; Ju, Z.; Zhu, Y.; Takeuchi, K. J.; Takeuchi, E. S.; Marschilok, A. C.; Yu, G. Multiscale understanding and architecture design of high energy/power lithium-ion battery electrodes. *Adv. Energy Mater.* **2021**, *11* (2), No. 2000808.
(5) Wang, Y.; Mijailovic, A. S.; Ji, T.; Cakmak, E.; Zhao, X.; Huang, L.; Sheldon, B. W.; Zhu, H. Promoting electrochemical rates by concurrent ionic-electronic conductivity enhancement in high mass loading cathode electrode. *Energy Storage Mater.* **2024**, *71*, No. 103546.
(6) Choi, J. W.; Aurbach, D. Promise and reality of post-lithium-ion batteries with high energy densities. *Nat. Rev. Mater.* **2016**, *1* (4), No. 16013.
(7) Li, P.; Kim, H.; Myung, S.-T.; Sun, Y.-K. Diverting exploration of silicon anode into practical way: a review focused on silicon-graphite composite for lithium ion batteries. *Energy Storage Mater.* **2021**, *35*, 550−576.
(8) Liu, N.; Lu, Z.; Zhao, J.; McDowell, M. T.; Lee, H.-W.; Zhao, W.; Cui, Y. A pomegranate-inspired nanoscale design for large-volume-change lithium battery anodes. *Nat. Nanotechnol.* **2014**, *9* (3), 187−192.
(9) Gao, S.; Wang, N.; Li, S.; Li, D.; Cui, Z.; Yue, G.; Liu, J.; Zhao, X.; Jiang, L.; Zhao, Y. A multi-wall Sn/SnO2@ carbon hollow nanofiber anode material for high-rate and long-life lithium-ion batteries. *Angew. Chem., Int. Ed.* **2020**, *59* (6), 2465−2472.
(10) Jia, B.; Chen, W.; Luo, J.; Yang, Z.; Li, L.; Guo, L. Construction of MnO2 artificial leaf with atomic thickness as highly stable battery anodes. *Adv. Mater.* **2020**, *32* (1), No. 1906582.
(11) Kwon, Y. H.; Minnici, K.; Park, J. J.; Lee, S. R.; Zhang, G.; Takeuchi, E. S.; Takeuchi, K. J.; Marschilok, A. C.; Reichmanis, E. SWNT anchored with carboxylated polythiophene "Links" on high-capacity Li-ion battery anode materials. *J. Am. Chem. Soc.* **2018**, *140* (17), 5666−5669.
(12) Wang, Y.; Luo, S.; Chen, M.; Wu, L. Uniformly confined germanium quantum dots in 3D ordered porous carbon framework for high-performance Li-ion battery. *Adv. Funct. Mater.* **2020**, *30* (16), No. 2000373.
(13) Zhu, R.; Wang, Z.; Hu, X.; Liu, X.; Wang, H. Silicon in hollow carbon nanospheres assembled microspheres cross-linked with N-doped carbon fibers toward a binder free, high performance, and flexible anode for lithium-ion batteries. *Adv. Funct. Mater.* **2021**, *31* (33), No. 2101487.
(14) Zhang, L.; Huang, Q.; Liao, X.; Dou, Y.; Liu, P.; Al-Mamun, M.; Wang, Y.; Zhang, S.; Zhao, S.; Wang, D. Scalable and controllable fabrication of CNTs improved yolk-shelled Si anodes with advanced in operando mechanical quantification. *Energy Environ. Sci.* **2021**, *14* (6), 3502−3509.
(15) Cheng, Z.; Jiang, H.; Zhang, X.; Cheng, F.; Wu, M.; Zhang, H. Fundamental Understanding and Facing Challenges in Structural Design of Porous Si-Based Anodes for Lithium-Ion Batteries. *Adv. Funct. Mater.* **2023**, No. 2301109.
(16) Ghaur, A.; Peschel, C.; Dienwiebel, I.; Haneke, L.; Du, L.; Profanter, L.; Gomez-Martin, A.; Winter, M.; Nowak, S.; Placke, T. Effective SEI Formation via Phosphazene-Based Electrolyte Additives for Stabilizing Silicon-Based Lithium-Ion Batteries. *Adv. Energy Mater.* **2023**, No. 2203503.
(17) Cheng, D.; Liu, Y.; Li, Z.; Rao, T.; Luo, D.; Zheng, P.; Guo, C.; Wang, J.; Pan, F.; Deng, Y.; Zeng, H.; Wang, C. An easy-to-prepare flexible 3D network aqueous binder with gradient hydrogen bonding for high-performance silicon anodes. *J. Power Sources* **2024**, *602*, No. 234328.
(18) Cheng, D.; Ni, P.; Qin, D.; Guo, Y.; Cai, S.; Liu, Y.; Rao, T.; Li, Y.; Wang, C. A water-based binder with 3D network enabling long-cycle-life silicon/graphite composite anode materials for lithium ion batteries. *Solid State Ionics* **2023**, *399*, No. 116289.
(19) Zhao, J.; Lu, Z.; Wang, H.; Liu, W.; Lee, H.-W.; Yan, K.; Zhuo, D.; Lin, D.; Liu, N.; Cui, Y. Artificial solid electrolyte interphase-protected Li x Si nanoparticles: an efficient and stable prelithiation reagent for lithium-ion batteries. *J. Am. Chem. Soc.* **2015**, *137* (26), 8372−8375.
(20) Yan, Y.; He, Y.-S.; Zhao, X.; Zhao, W.; Ma, Z.-F.; Yang, X. Regulating adhesion of solid-electrolyte interphase to silicon via covalent bonding strategy towards high Coulombic-efficiency anodes. *Nano Energy* **2021**, *84*, No. 105935.
(21) Ryu, J.; Hong, D.; Shin, M.; Park, S. Multiscale hyperporous silicon flake anodes for high initial coulombic efficiency and cycle stability. *ACS Nano* **2016**, *10* (11), 10589−10597.
(22) Sun, L.; Liu, Y.; Shao, R.; Wu, J.; Jiang, R.; Jin, Z. Recent progress and future perspective on practical silicon anode-based lithium ion batteries. *Energy Storage Mater.* **2022**, *46*, 482−502.
(23) Liu, X. H.; Zhong, L.; Huang, S.; Mao, S. X.; Zhu, T.; Huang, J. Y. Size-dependent fracture of silicon nanoparticles during lithiation. *ACS Nano* **2012**, *6* (2), 1522−1531.
(24) Kim, H.; Seo, M.; Park, M. H.; Cho, J. A critical size of silicon nano-anodes for lithium rechargeable batteries. *Angew. Chem., Int. Ed.* **2010**, *49* (12), 2146−2149.
(25) Cho, J.-H.; Picraux, S. T. Enhanced lithium ion battery cycling of silicon nanowire anodes by template growth to eliminate silicon underlayer islands. *Nano Lett.* **2013**, *13* (11), 5740−5747.
(26) Ryu, J.; Hong, D.; Choi, S.; Park, S. Synthesis of ultrathin Si nanosheets from natural clays for lithium-ion battery anodes. *ACS Nano* **2016**, *10* (2), 2843−2851.
(27) Jeong, Y. K.; Huang, W.; Vilá, R. A.; Huang, W.; Wang, J.; Kim, S. C.; Kim, Y. S.; Zhao, J.; Cui, Y. Microclusters of kinked silicon nanowires synthesized by a recyclable iodide process for high-performance lithium-ion battery anodes. *Adv. Energy Mater.* **2020**, *10* (41), No. 2002108.
(28) Ge, G.; Li, G.; Wang, X.; Chen, X.; Fu, L.; Liu, X.; Mao, E.; Liu, J.; Yang, X.; Qian, C. Manipulating oxidation of silicon with fresh surface enabling stable battery anode. *Nano Lett.* **2021**, *21* (7), 3127−3133.
(29) Yang, Y.; Lu, Z.; Xia, J.; Liu, Y.; Wang, K.; Wang, X. Crystalline and amorphous carbon double-modified silicon anode: Towards large-scale production and superior lithium storage performance. *Chem. Eng. Sci.* **2021**, *229*, No. 116054.
(30) Jia, H.; Li, X.; Song, J.; Zhang, X.; Luo, L.; He, Y.; Li, B.; Cai, Y.; Hu, S.; Xiao, X. Hierarchical porous silicon structures with extraordinary mechanical strength as high-performance lithium-ion battery anodes. *Nat. Commun.* **2020**, *11* (1), No. 1474.
(31) Ren, Y.; Xiang, L.; Yin, X.; Xiao, R.; Zuo, P.; Gao, Y.; Yin, G.; Du, C. Ultrathin Si nanosheets dispersed in graphene matrix enable stable interface and high rate capability of anode for lithium-ion batteries. *Adv. Funct. Mater.* **2022**, *32* (16), No. 2110046.
(32) Shen, X.; Tian, Z.; Fan, R.; Shao, L.; Zhang, D.; Cao, G.; Kou, L.; Bai, Y. Research progress on silicon/carbon composite anode materials for lithium-ion battery. *J. Energy Chem.* **2018**, *27* (4), 1067−1090.
(33) Hu, Y. S.; Demir-Cakan, R.; Titirici, M. M.; Müller, J. O.; Schlögl, R.; Antonietti, M.; Maier, J. Superior storage performance of

https://doi.org/10.1021/acsaem.4c01132
ACS Appl. Energy Mater. 2024, 7, 7220−7231

a Si@ SiOx/C nanocomposite as anode material for lithium-ion batteries. *Angew. Chem., Int. Ed.* **2008**, *47* (9), 1645−1649.
(34) Nava, G.; Schwan, J.; Boebinger, M. G.; McDowell, M. T.; Mangolini, L. Silicon-core−carbon-shell nanoparticles for lithium-ion batteries: rational comparison between amorphous and graphitic carbon coatings. *Nano Lett.* **2019**, *19* (10), 7236−7245.
(35) Gueon, D.; Moon, J. H. Polydopamine-wrapped, silicon nanoparticle-impregnated macroporous CNT particles: rational design of high-performance lithium-ion battery anodes. *Chem. Commun.* **2019**, *55* (3), 361−364.
(36) Yang, J.; Wang, Y.-X.; Chou, S.-L.; Zhang, R.; Xu, Y.; Fan, J.; Zhang, W.-x.; Liu, H. K.; Zhao, D.; Dou, S. X. Yolk-shell silicon-mesoporous carbon anode with compact solid electrolyte interphase film for superior lithium-ion batteries. *Nano Energy* **2015**, *18*, 133−142.
(37) Tan, W.; Yang, F.; Yi, T.; Liu, G.; Wei, X.; Long, Q.; Liu, Y.; Li, Y.; Guo, C.; Liu, K. Fullerene-like elastic carbon coatings on silicon nanoparticles by solvent controlled association of natural polyaromatic molecules as high-performance lithium-ion battery anodes. *Energy Storage Mater.* **2022**, *45*, 412−421.
(38) Sun, Z.; Khau, B.; Dong, H.; Takacs, C. J.; Yuan, S.; Sun, M.; Mosevitzky Lis, B.; Nguyen, D.; Reichmanis, E. Carboxyl-Alkyl Functionalized Conjugated Polyelectrolytes for High Performance Organic Electrochemical Transistors. *Chem. Mater.* **2023**, *35*, 9299−9312.
(39) Khau, B. V.; Savagian, L. R.; De Keersmaecker, M.; Gonzalez, M. A.; Reichmanis, E. Carboxylic Acid Functionalization Yields Solvent-Resistant Organic Electrochemical Transistors. *ACS Mater. Lett.* **2019**, *1* (6), 599−605.
(40) Ren, H.; Takeuchi, E. S.; Marschilok, A. C.; Takeuchi, K. J.; Reichmanis, E. Enhancing composite electrode performance: insights into interfacial interactions. *Chem. Commun.* **2024**, *60*, 1979−1998.
(41) Kwon, Y. H.; Minnici, K.; Lee, S. R.; Zhang, G.; Takeuchi, E. S.; Takeuchi, K. J.; Marschilok, A. C.; Reichmanis, E. SWNT Networks with Polythiophene Carboxylate Links for High-Performance Silicon Monoxide Electrodes. *ACS Appl. Energy Mater.* **2018**, *1* (6), 2417−2423.
(42) Na, R.; Minnici, K.; Zhang, G.; Lu, N.; González, M. A.; Wang, G.; Reichmanis, E. Electrically conductive shell-protective layer capping on the silicon surface as the anode material for high-performance lithium-ion batteries. *ACS Appl. Mater. Interfaces* **2019**, *11* (43), 40034−40042.
(43) Feng, K.; Li, M.; Liu, W.; Kashkooli, A. G.; Xiao, X.; Cai, M.; Chen, Z. Silicon-based anodes for lithium-ion batteries: from fundamentals to practical applications. *Small* **2018**, *14* (8), No. 1702737.
(44) Zhu, G.; Chao, D.; Xu, W.; Wu, M.; Zhang, H. Microscale silicon-based anodes: fundamental understanding and industrial prospects for practical high-energy lithium-ion batteries. *ACS Nano* **2021**, *15* (10), 15567−15593.
(45) Kwon, Y. H.; Park, J. J.; Housel, L. M.; Minnici, K.; Zhang, G.; Lee, S. R.; Lee, S. W.; Chen, Z.; Noda, S.; Takeuchi, E. S. Carbon nanotube web with carboxylated polythiophene "assist" for high-performance battery electrodes. *ACS Nano* **2018**, *12* (4), 3126−3139.
(46) Zhou, X.; Yin, Y. X.; Wan, L. J.; Guo, Y. G. Self-assembled nanocomposite of silicon nanoparticles encapsulated in graphene through electrostatic attraction for lithium-ion batteries. *Adv. Energy Mater.* **2012**, *2* (9), 1086−1090.
(47) Kwon, Y. H.; Park, J. J.; Housel, L. M.; Minnici, K.; Zhang, G.; Lee, S. R.; Lee, S. W.; Chen, Z.; Noda, S.; Takeuchi, E. S.; Takeuchi, K. J.; Marschilok, A. C.; Reichmanis, E. Carbon Nanotube Web with Carboxylated Polythiophene "Assist" for High-Performance Battery Electrodes. *ACS Nano* **2018**, *12* (4), 3126−3139.
(48) Chen, Y.; Liu, L.; Xiong, J.; Yang, T.; Qin, Y.; Yan, C. Porous Si nanowires from cheap metallurgical silicon stabilized by a surface oxide layer for lithium ion batteries. *Adv. Funct. Mater.* **2015**, *25* (43), 6701−6709.
(49) Zhang, L.; Deng, J.; Liu, L.; Si, W.; Oswald, S.; Xi, L.; Kundu, M.; Ma, G.; Gemming, T.; Baunack, S. Hierarchically designed SiOx/SiOy bilayer nanomembranes as stable anodes for lithium ion batteries. *Adv. Mater.* **2014**, *26* (26), 4527−4532.
(50) Chen, S.; Shen, L.; van Aken, P. A.; Maier, J.; Yu, Y. Dual-functionalized double carbon shells coated silicon nanoparticles for high performance lithium-ion batteries. *Adv. Mater.* **2017**, *29* (21), No. 1605650.
(51) Liu, H.; Chen, T.; Xu, Z.; Liu, Z.; Yang, J.; Chen, J. High-safety and long-life silicon-based lithium-ion batteries via a multifunctional binder. *ACS Appl. Mater. Interfaces* **2020**, *12* (49), 54842−54850.
(52) Ai, Q.; Li, D.; Guo, J.; Hou, G.; Sun, Q.; Sun, Q.; Xu, X.; Zhai, W.; Zhang, L.; Feng, J. Artificial Solid Electrolyte Interphase Coating to Reduce Lithium Trapping in Silicon Anode for High Performance Lithium-Ion Batteries. *Adv. Mater. Interfaces* **2019**, *6* (21), No. 1901187.
(53) Levi, M. D.; Aurbach, D. The mechanism of lithium intercalation in graphite film electrodes in aprotic media. Part 1. High resolution slow scan rate cyclic voltammetric studies and modeling. *J. Electroanal. Chem.* **1997**, *421* (1−2), 79−88.
(54) Li, A.-M.; Wang, Z.; Pollard, T. P.; Zhang, W.; Tan, S.; Li, T.; Jayawardana, C.; Liou, S. C.; Rao, J.; Lucht, B. L.; Hu, E.; Yang, X. Q.; Borodin, O.; Wang, C. High voltage electrolytes for lithium-ion batteries with micro-sized silicon anodes. *Nat. Commun.* **2024**, *15* (1), No. 1206.
(55) Forney, M. W.; Ganter, M. J.; Staub, J. W.; Ridgley, R. D.; Landi, B. J. Prelithiation of silicon−carbon nanotube anodes for lithium ion batteries by stabilized lithium metal powder (SLMP). *Nano Lett.* **2013**, *13* (9), 4158−4163.
(56) Tian, R.; Park, S. H.; King, P. J.; Cunningham, G.; Coelho, J.; Nicolosi, V.; Coleman, J. N. Quantifying the factors limiting rate performance in battery electrodes. *Nat. Commun.* **2019**, *10* (1), No. 1933.
(57) Ren, H.; Wang, Y.; Cao, D.; Gedney, W.; Ji, T.; Sun, X.; Zhu, H. Manufacturing Water-Based Low-Tortuosity Electrodes for Fast-Charge through Pattern Integrated Stamping. *Energy Environ. Mater.* **2023**, *6*, No. e12584.
(58) Liu, N.; Wu, H.; McDowell, M. T.; Yao, Y.; Wang, C.; Cui, Y. A yolk-shell design for stabilized and scalable li-ion battery alloy anodes. *Nano Lett.* **2012**, *12* (6), 3315−3321.
(59) Zhang, L.; Jiao, X.; Feng, Z.; Li, B.; Feng, Y.; Song, J. A nature-inspired binder with three-dimensional cross-linked networks for silicon-based anodes in lithium-ion batteries. *J. Power Sources* **2021**, *484*, No. 229198.
(60) Ge, M.; Lu, Y.; Ercius, P.; Rong, J.; Fang, X.; Mecklenburg, M.; Zhou, C. Large-scale fabrication, 3D tomography, and lithium-ion battery application of porous silicon. *Nano Lett.* **2014**, *14* (1), 261−268.
(61) An, Y.; Han, X.; Liu, Y.; Azhar, A.; Na, J.; Nanjundan, A. K.; Wang, S.; Yu, J.; Yamauchi, Y. Progress in Solid Polymer Electrolytes for Lithium-Ion Batteries and Beyond. *Small* **2022**, *18* (3), No. e2103617.
(62) Imtiaz, S.; Amiinu, I. S.; Storan, D.; Kapuria, N.; Geaney, H.; Kennedy, T.; Ryan, K. M. Dense Silicon Nanowire Networks Grown on a Stainless-Steel Fiber Cloth: A Flexible and Robust Anode for Lithium-Ion Batteries. *Adv. Mater.* **2021**, *33* (52), No. 2105917.
(63) Zhang, Q.; Xiao, X.; Zhou, W.; Cheng, Y. T.; Verbrugge, M. W. Toward High Cycle Efficiency of Silicon-Based Negative Electrodes by Designing the Solid Electrolyte Interphase. *Adv. Energy Mater.* **2015**, *5* (5), No. 1401398.
(64) Cao, Z.; Zheng, X.; Huang, W.; Wang, Y.; Qu, Q.; Zheng, H. Dynamic bonded supramolecular binder enables high-performance silicon anodes in lithium-ion batteries. *J. Power Sources* **2020**, *463*, No. 228208.
(65) Yang, Q.; Li, C. Li metal batteries and solid state batteries benefiting from halogen-based strategies. *Energy Storage Mater.* **2018**, *14*, 100−117.
(66) Zhao, H.; Liang, K.; Wang, S.; Ding, Z.; Huang, X.; Chen, W.; Ren, Y.; Li, J. A Stress Self-Adaptive Silicon/Carbon "Ordered Structures" to Suppress the Electro-Chemo-Mechanical Failure:

https://doi.org/10.1021/acsaem.4c01132
ACS Appl. Energy Mater. 2024, 7, 7220−7231

Piezo-Electrochemistry and Piezo-Ionic Dynamics. *Adv. Sci.* **2023**, *10*, No. 2303696.
(67) He, Z.; Xiao, Z.; Yue, H.; Jiang, Y.; Zhao, M.; Zhu, Y.; Yu, C.; Zhu, Z.; Lu, F.; Jiang, H.; Zhang, C.; Wei, F. Single-Walled Carbon Nanotube Film as an Efficient Conductive Network for Si-Based Anodes. *Adv. Funct. Mater.* **2023**, *33*, No. 2300094.
(68) Bai, Y.; Zhang, R.; Ye, X.; Zhu, Z.; Xie, H.; Shen, B.; Cai, D.; Liu, B.; Zhang, C.; Jia, Z.; Zhang, S.; Li, X.; Wei, F. Carbon nanotube bundles with tensile strength over 80 GPa. *Nat. Nanotechnol.* **2018**, *13* (7), 589−595.
(69) Sun, C. F.; Zhu, H.; Okada, M.; Gaskell, K.; Inoue, Y.; Hu, L.; Wang, Y. Interfacial oxygen stabilizes composite silicon anodes. *Nano Lett.* **2015**, *15* (1), 703−708.

https://doi.org/10.1021/acsaem.4c01132
ACS Appl. Energy Mater. 2024, 7, 7220−7231